

# Experimental Investigation of AoA Estimation and Antenna Calibration With 5G NR Signals Using USRP Devices

Alda Xhafa<sup>1</sup>, Member, IEEE, Fran Fabra<sup>1</sup>, Daniel Egea-Roca<sup>1</sup>, Member, IEEE, José A. López-Salcedo<sup>1</sup>, Senior Member, IEEE, and Gonzalo Seco-Granados<sup>1</sup>, Fellow, IEEE

**Abstract**—The advent of 5G technology has significantly advanced the capability of centimeter-level positioning, with angle of arrival (AoA) estimation emerging as a key technique to achieve this level of accuracy. This article presents a software receiver based on universal software radio peripheral (USRP) devices, designed for precise Angle of Arrival (AoA) estimation using 5G new radio (NR) signals, especially in challenging environments. The proposed receiver addresses critical issues, such as hardware and antenna calibration, synchronization, and signal processing, enabling accurate angle estimation in both outdoor and indoor environments. The study explores the impact of hardware imperfections, antenna errors, and environmental factors, including multipath propagation, on angle estimation accuracy. Our approach combines AoA estimation with calibration techniques, demonstrating the feasibility of delivering reliable, high-precision location-based services with 5G signals. Through a combination of simulation and real-world experiments, we assess the performance of the system in scenarios with and without multipath interference, including the influence of reflectors on AoA measurements. The results provide a valuable foundation for advancing the understanding and implementation of precise AoA estimation and calibration using 5G New Radio (NR) signals and Universal Software Radio Peripheral (USRP) devices.

**Index Terms**—5G, angle of arrival (AOA), array calibration, coherent phase, multipath, SDR, synchronization.

## I. INTRODUCTION

**I**N RECENT years, the rapid development of technologies, such as indoor navigation [1], [2], autonomous driving [3], healthcare, intelligent transportation, and the Industrial Internet of Things (IIoT) [4], [5] has driven a growing demand for accurate location information. Achieving centimeter-level accuracy has become a priority, requiring specialized hardware and techniques [6]. While precise positioning has traditionally

relied on satellite-based systems like global positioning system (GPS), there is a rising interest in using cellular networks [7], [8], [9] to provide more reliable location awareness [10], especially in challenging environments such as indoor spaces and urban canyons [11], [12]. The deployment of 5G small-cell base stations in areas with poor or no global navigation Satellite system (GNSS) coverage offers a promising solution for achieving precise localization [13]. High-frequency bands, such as millimeter-wave [14], [15], [16] and subterahertz [17], [18], present significant advantages for positioning by improving spatial resolution and enabling efficient resource allocation for both communication and localization. Among the various positioning techniques, angle of arrival (AoA) estimation, which has been incorporated into the 5G new radio (NR) standard [19], [20], [21], is gaining attention due to its ability to provide accurate position information without the need for precise timing synchronization. This capability makes Angle of Arrival (AoA) particularly effective for single-site positioning, where a user's location is determined using measurements from only one base station [22], [23], [24]. By utilizing AoA information for positioning [13], [25], [26], [27], cellular networks can enhance the precision of location-based services while reducing the infrastructure requirements.

Several numerical simulations and experimental studies [21], [28], [29], [30], [31] have demonstrated the potential for high-precision position estimation using AoA measurements. However, these studies often overlook the practical challenges encountered in real-world implementations. The accuracy of angle estimation is highly sensitive to hardware impairments, clock stability, synchronization, and phase misalignment. Additionally, factors such as manufacturing inaccuracies, temperature variations, hardware-related issues, environmental conditions, and time-frequency misalignment between the transmitter and receiver contribute to the degradation of AoA estimation accuracy and eventually the localization performance.

To mitigate the issues mentioned earlier, various research efforts have been conducted. Several works have studied the impact of hardware impairments on AoA estimation [32], [33], [34], [35], [36], [37], [38]. For instance, studies such as [32], [33], [34], [35] consider gain-phase errors from radio frequency (RF) channels but assume ideal array models. In practice, however, real-world antenna arrays are affected by

Received 2 October 2024; revised 31 January 2025; accepted 21 March 2025. Date of publication 12 May 2025; date of current version 30 May 2025. This work was supported in part by the grant PID2023-152820OB-I00 funded by MICIU/AEI/10.13039/501100011033 and ERDF/EU; the grant PDC2023-145858-I00 funded by MICIU/AEI/10.13039/501100011033 and the European Union NextGenerationEU/PRTR; and the AGAUR-ICREA Academia Programme. The Associate Editor coordinating the review process was Dr. Jingyu Hua. (*Corresponding author: Alda Xhafa.*)

The authors are with the Department of Telecommunications and Systems Engineering, IIEC-CERES, Universitat Autònoma de Barcelona, Bellaterra, 08193 Barcelona, Spain (e-mail: alda.xhafa@uab.cat; franciscojose.fabra@uab.cat; daniel.egea@uab.cat; jose.salcedo@uab.cat; gonzalo.seco@uab.cat).

Digital Object Identifier 10.1109/TIM.2025.3569347

imperfections, commonly referred to as array errors. These deviations from the theoretical array manifold highlight the necessity of accurately calibrating arrays by estimating these errors and determining the true array manifold. While [32], [33], [34], [35] offer limited details about the effect of hardware impairments on angle estimation, this issue is thoroughly analyzed in [36], which also considers its impact on localization. However, practical methods for overcoming these impairments in real-world implementations are not addressed. The study in [37] explores practical implementation challenges, such as nonuniform radiation pattern among antenna elements and discrepancies in the characteristics of Radio Frequency (RF) front-ends, antenna feed cables, connectors, and other RF components. Yet, it too lacks practical solutions for mitigating these impairments. In [38], both antenna and gain-phase error calibration are considered, though the effectiveness of their in situ antenna calibration is limited to the specific environment in which it is performed, reducing its applicability to other settings due to environmental sensitivity.

Another important note is that most of the previously mentioned studies rely on classical AoA estimation techniques, such as Beamforming [39], multiple signal classification (MUSIC) [40], and estimation of signal parameters via rotational invariance techniques (ESPRIT) [41], which may be unsuitable for challenging environments. These conventional algorithms face difficulties when dealing with coherent signals, as they cause rank deficiencies in the source covariance matrix and require more antenna elements than the number of incoming signals. Moreover, these methods typically demand a large number of snapshots and high signal-to-noise ratio (SNR) for accurate spatial resolution, which is impractical in rapidly changing or low-Signal-to-Noise Ratio (SNR) environments. Subspace-based techniques, even with array calibration, are sensitive to source coherence due to their reliance on subspace orthogonality. Therefore, it is important to explore alternative approaches, such as parameter-free iterative methods (e.g., iterative adaptive approaches (IAA) [42], [43], Sparse Asymptotic Minimum Variance (SAMV) [44], [45], [46], and sparse asymptotic minimum variance (SAMV) [46]), which are effective with a limited number of snapshots and show robustness to coherent sources. However, techniques like Iterative Adaptive Approaches (IAA) and SAMV are computationally intensive, though SAMV-Stochastic ML (SAMV-SML) offers reduced complexity by being grid-limit-free. Nevertheless, SAMV-SML is highly sensitive to initial conditions. While these advanced methods aim to improve localization robustness, their effectiveness must be validated not only through simulations but also in experimental setups beyond ideal conditions. Current testbeds [35], [38], [47] do not provide a complete end-to-end system for accurate estimation with 5G signals. Tailored compensation methods are needed for 5G systems, as the hardware impairments in these networks differ from those in other systems. To address these challenges, the key contributions of this work are.

- 1) The development of a software receiver for AoA estimation using emulated 5G signals. The end-to-end testbed uses universal software radio peripheral (USRP) devices, taking into account hardware impairments, antenna cal-

ibration, and the required synchronization processes for 5G New Radio (NR) orthogonal frequency division multiplexing (OFDM) signals. Thanks to the adaptability and software support of the Universal Software Radio Peripheral (USRP) devices, the proposed system is a customizable RF testbed, allowing experiments with different parameter configurations, such as carrier frequency, sampling rate, and gain.

- 2) A detailed analysis of alternative AoA estimation methods, such as parameter-free iterative approaches, compared to classical AoA techniques from the literature. Their performance is evaluated through simulations and experiments under complex channel conditions, such as multipath propagation, closely spaced signals, and coherent sources across varying SNR levels. Additionally, we incorporate antenna error corrections into the estimation algorithms, addressing the limitations of ideal array steering vector assumptions.
- 3) The integration of RF and antenna array calibration into AoA estimation process to minimize the systematic errors and therefore improve the accuracy. This dual-calibration approach allows to achieve a significant reduction of error estimation compared to conventional methods that apply only single or omit the calibration entirely [29], [30].
- 4) A comprehensive reference for computing observables (i.e., angles) when working with 5G signals. While 5G standards define aspects such as positioning estimation, signal generation, and channel models, they do not specify a standardized methodology for observable computations. This is particularly important in experimental scenarios where hardware impairments and synchronization errors must be accounted for.
- 5) Experimental validation exploring enhancements in AoA estimation and assessing angle error performance in environments with significant multipath and interference, ensuring robust and reliable AoA estimation.

The structure of the article is as follows. Section II describes the signal transmission system for the proposed end-to-end AoA estimation framework. This section includes details on the signal structure, configuration, and the transmission module, covering waveform generation and transmission. Section III outlines the structure of the proposed receiver, providing a detailed explanation of each system stage: signal acquisition, synchronization module, calibration module, signal demodulation and extraction, and AoA estimation block. The synchronization process addresses challenges specific to Orthogonal Frequency Division Multiplexing (OFDM) systems, where synchronization errors can compromise subcarrier orthogonality, negatively affecting angle estimation accuracy. The calibration module includes both RF channel and antenna error calibration. The RF channel calibration focuses on ensuring coherent phase reception across all RF channels, while the antenna calibration is conducted in a controlled environment, using a measurement chamber to eliminate multipath propagation and interference. Section IV provides an in-depth simulation analysis, exploring the impact of synchronization errors on AoA estimation accuracy and angular precision, as

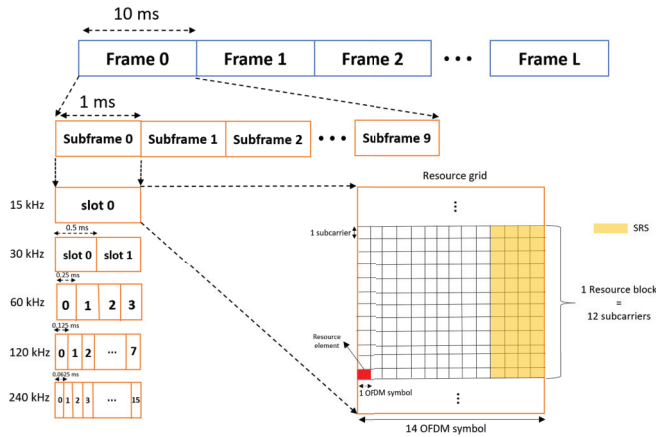


Fig. 1. Example of 5G Frame structure. The last four symbols of each slot are allocated to Sounding Reference Signal (SRS). SRS is transmitted every two subcarriers.

well as the effects of multipath interference. Section V presents the experimental validation, detailing a testbed based on versatile USRP devices. This section reports the performance of AoA estimation in both Line of Sight (LoS) conditions and scenarios with the presence of a reflector. Finally, Section VI provides the paper's conclusion.

## II. SIGNAL TRANSMISSION SYSTEM

### A. Signal Structure

In this work, we focus on the 5G uplink sounding reference signal (SRS) signal, which is based on OFDM modulation with cycle prefix (CP). The uplink waveform generation process follows the specifications set by the generation partnership project (3GPP) standard as outlined in [48], which defines the cellular network standards for both current 5G and future 6G frameworks, particularly in location-based services. The 5G waveform is organized into frames of 10 ms duration, with each divided into 10 subframes of 1 ms, called slots, as illustrated in Fig. 1. Each frame in the time domain contains multiple slots, with each slot consisting of 14 OFDM symbols for normal Cycle Prefix (CP) length, or 12 symbols when using an extended CP. The number of slots per subframe depends on the subcarrier spacing, which 5G defines through different numerologies  $\mu \in \{0, \dots, 4\}$  to support flexible subcarrier spacing  $\Delta f = 2^\mu 15$  kHz. As numerology increases, the number of slots per subframe also increases, and consequently, the number of OFDM symbols varies, resulting in shorter slot durations with wider subcarrier spacings, an inherent characteristic of OFDM. For subcarrier spacings, 15 and 30 kHz are more suitable for frequency range 1 (FR1) due to lower signal attenuation and larger cell sizes, while higher subcarrier spacings are more appropriate for frequency range 2 (FR2). In the frequency domain, each subframe is divided into resource grids, which are composed of multiple resource blocks. Each resource block consists of 12 consecutive subcarriers, representing the smallest defined unit in the grid, corresponding to a single OFDM subcarrier over a single OFDM symbol interval.

### B. Signal Transmission

The signal transmission module includes both waveform generation and transmission. The 5G waveform generation process begins with data modulation, as depicted in the *Signal transmission* block in Fig. 2. In this step, data are converted into symbols through symbol mapping. The resulting waveform is structured as described in Section II-A, with the OFDM symbols converted from serial to parallel format using a series-to-parallel converter. Each subcarrier to [resource element (RE)] is then mapped within the frequency domain across the allocated transmission resources. A frequency gap of two subcarriers is maintained between successive pilots for each SRS symbol, with the separation predefined by the numerology. This comb structure, with a gap of 2, ensures high density in the time domain. The transmitted Resource Element (RE) are mapped to all available subcarriers per symbol. Following this process, each symbol undergoes OFDM modulation by applying an inverse fast Fourier transform (IFFT) to convert the frequency-domain pilot data into time-domain OFDM data symbols for transmission. During this process, a CP with a length of  $N_{cp}$  is added to each of the OFDM symbols within the slot. A maximum of 4 SRS symbols can be assigned per slot. The digital baseband signal of the  $l$ th OFDM symbol in the time domain is expressed as

$$x^l[n] = \frac{1}{N} \sum_{k=-\frac{N}{2}}^{\frac{N}{2}-1} b^l[k] e^{j \frac{2\pi k(n-N_{cp})}{N}} \quad (1)$$

where  $n = 0, 1, \dots, N+N_{cp}-1$  is the sample index of an OFDM symbol, and  $k$  is the OFDM subcarrier index. The generated waveform is stored in a binary file, where the In-phase and quadrature (I/Q) samples are interleaved. Transmission occurs periodically, with  $N_{slot}$  slots sent in each transmission cycle. The signal is transmitted in a predefined AoA and is received by the uniform linear array (ULA) antenna system with linearly spaced  $M$  omnidirectional antennas, separated by an equal distance  $d$ , as shown in Fig. 3. Each Uniform Linear Array (ULA) element captures the signal from the  $u$ th source, which impinges on the array at an angle  $\theta_u$ , enabling AoA estimation.

## III. RECEIVER STRUCTURE

The receiver software consists of several components (see Fig. 4), including signal acquisition, calibration, synchronization, signal demodulation and extraction, and AoA estimation modules. The signal acquisition module captures the RF signals received by the hardware (e.g., USRP). Each radio channel provides a separate baseband stream, all configured with common parameters, and the captured signals are stored for subsequent processing. The calibration module includes both RF channel calibration and antenna error calibration. RF channel calibration, applied immediately after signal acquisition, corrects phase misalignment between the receiver's RF channels. Antenna error calibration, performed at the final stage, compensates for offsets between antenna elements and is integrated into the angle estimation algorithms. The synchronization module employs both coarse and fine methods

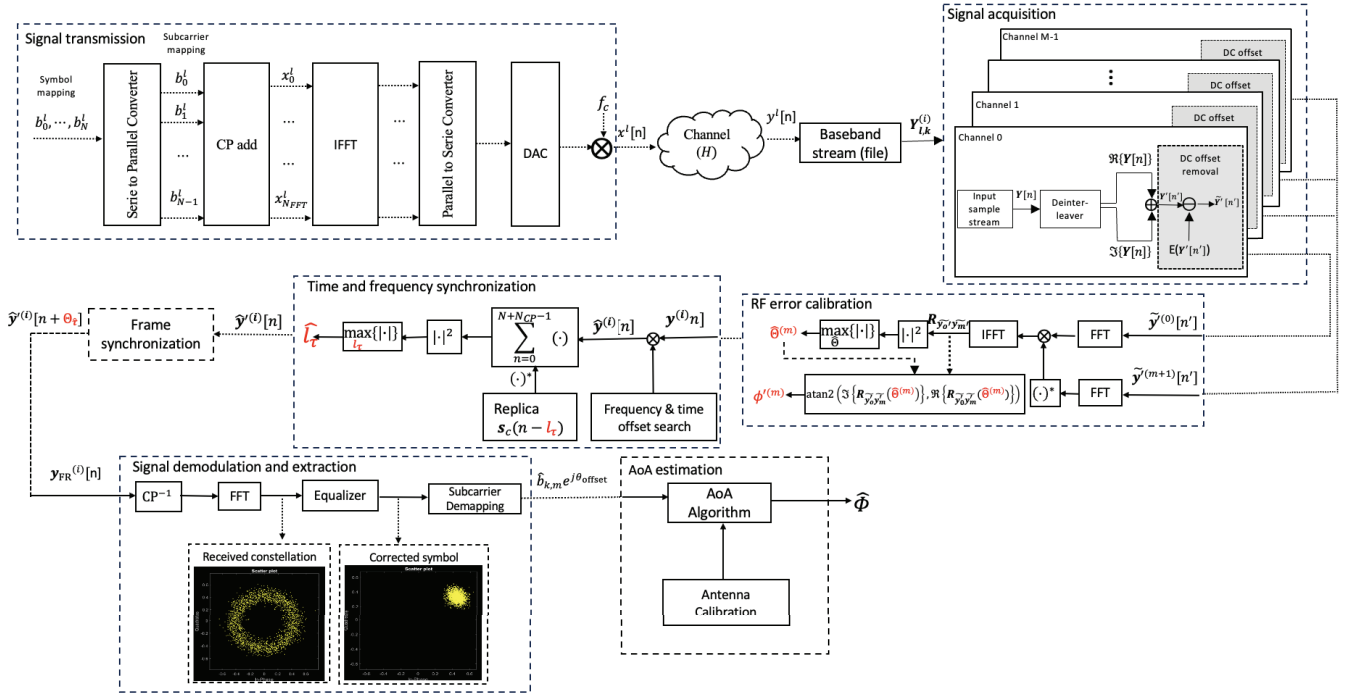


Fig. 2. Block diagram of AoA estimation, illustrating signal transmission and reception. The reception process includes signal acquisition, calibration, synchronization, demodulation, and angle estimation, while accounting for hardware impairments, antenna errors, and synchronization inaccuracies.

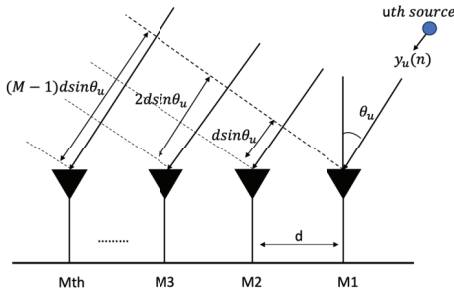


Fig. 3. ULA with M elements for AoA estimation.

to estimate time delay and frequency offset, using known pilot symbols transmitted by the sender. These corrections occur after compensating for hardware impairments through RF channel calibration. The signal demodulation and extraction block processes the corrected waveforms, demodulates them, and applies an fast Fourier transform (FFT) to extract OFDM symbols containing pilot signals, which are then used for AoA estimation. Each stage plays a crucial role in ensuring accurate AoA estimation. The following sections provide a detailed description of each stage, accompanied by corresponding diagrams for further clarity, as depicted in Fig. 2.

### A. Signal Acquisition

The signal acquisition module captures the transmitted waveforms at each of the radio channels of the receiver platform (see *Signal acquisition* block in Fig. 2). In reception, the signal stream corresponding to the  $i$ th received radio channel of the receiver at the  $l$ th OFDM symbol, and the  $k$ th

subcarrier, is denoted as

$$Y_{l,k}^{(i)} = a^{(i)}(\theta)b_{l,k}^{(i)}e^{-\frac{j2\pi(k\tau + l\varepsilon)}{N}}e^{j\Phi^{(i)}}e^{j\beta^{(i)}} + w_{l,k}^{(i)} \quad (2)$$

where  $a(\theta) = \sqrt{\alpha(\theta)}e^{j\Phi(\theta)}$  is the antenna response at  $i$ th front-end channel composed by the gain pattern  $\alpha(\theta)$  and phase pattern  $\Phi(\theta)$ ,  $\tau$  is the time delay, and  $\varepsilon$  is the carrier frequency offset (CFO). The phase offset  $\Phi'$  represents the hardware-induced phase offset of the  $i$ th received RF channel. Additionally,  $\beta$  encompasses the remaining phase offsets influencing the error in the  $i$ th antenna response of the corresponding RF channel. These offsets may arise from factors such as antenna nonidealities, surrounding structures, multipath, and/or interference. Finally,  $w_{l,k}^{(i)}$  denotes the noise of  $i$ th channel at the  $l$ th OFDM symbol and  $k$ th subcarrier. Each radio channel of the receiver corresponds to a distinct baseband received signal provided by the hardware front end. These signals are organized into a single matrix  $\mathbf{G} = [\mathbf{y}_1, \mathbf{y}_2, \dots, \mathbf{y}_M]^T \in \mathbb{C}^{M,N}$  during acquisition. The received baseband stream is separated so that each radio channel has its baseband stream from the hardware front-end. The stream of each radio channel goes through a deinterleaver, which rearranges the order of previously interleaved data. The data are then subtracted from the average value of the signal itself. This process effectively eliminates the dc offset, a constant bias that could affect subsequent processing steps, ensuring that the signal is centered around zero.

### B. Calibration

One of the main sources of error in signal reception originates from hardware- and antenna-related factors. Moreover, the radio environment introduces additional issues, such as



Fig. 4. Illustration of the receiver top-level block diagram.

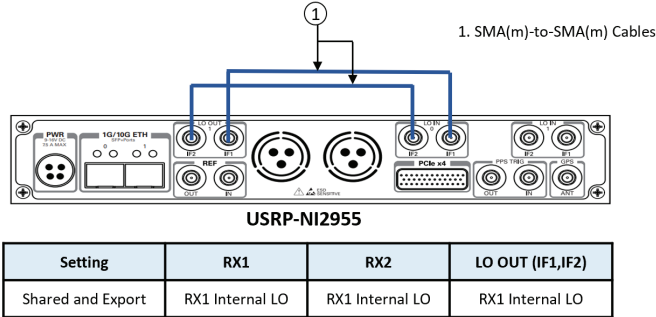


Fig. 5. Phase alignment between the four-channel receiver of the USRP NI2955 using LO sharing connection.

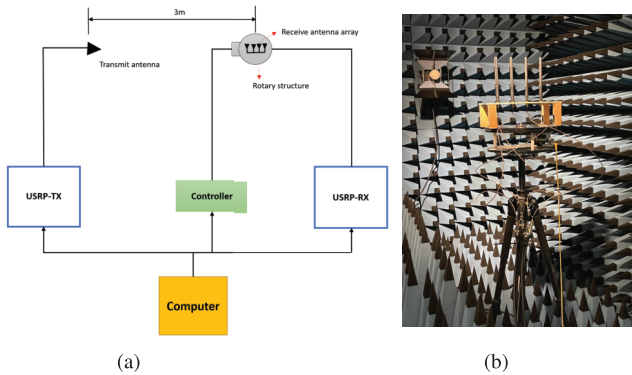


Fig. 6. Antenna array manifold calibration process in a controlled environment (i.e., anechoic chamber). (a) Antenna calibration method. (b) Anechoic chamber.

multipath and interference. This section describes primary calibration procedures: RF channel error calibration (see Fig. 5 and *RF error calibration* block in Fig. 2), and antenna error calibration (see Fig. 6). The calibration process uses the same 5G NR signal as the experiments. RF channel calibration is performed by directly connecting the transmitter (USRP N310) to the receiver (USRP NI-2955) via coaxial cables and a power splitter, ensuring an undistorted signal for measuring phase and timing offsets between RF channels. These cables also connect the receiver's antenna elements for both calibration and experimentation. System parameters, including carrier frequency, sampling rate, and transmission gain, remain consistent throughout. Both calibration processes affect the accuracy of angle estimation.

1) *RF Channel Error Calibration*: The calibration of RF channels is crucial for ensuring coherent phase reception across multiple RF channels of the Software-Defined Radio (SDR) device. In this way, it will ensure compensation for hardware imperfections. The process of RF calibration varies depending on the model of multichannel SDR platforms used. For instance, the focus here is on USRP devices, which are

widely adopted in high-end developments due to their large FPGA and flexibility to meet RF requirements. This article will use model N310 [49] as a transmitter and model NI-2955 [50] as a receiver. These USRP models are chosen because they allow the use of the required sampling rate and bandwidth for the experimental setup presented in Section V. To ensure phase-aligned operation, the configuration of the multichannel receiver enables local oscillator (LO) sharing among channels across multiple daughter boards. This is achieved by exporting the Local Oscillator (LO) output from the initial pair of channels to the second pair of channels via external cables connected to the respective LO ports as shown in Fig. 5. Another factor influencing phase alignment is the sampling rate. To maintain precise alignment, the signals received by all front ends must be sampled simultaneously. For a more detailed description of the calibration process and its impact, please refer to [51].

The phase offset between RF channels is estimated by performing the circular correlation of the received signal of the first RF channel  $\tilde{y}^{(0)}[n']$ , where  $m = 0$ , with the rest of the received signals  $\tilde{y}^{(m)}[n']$ , where  $m = 1, 2, \dots, M - 1$ , at the receiver side as

$$R_{\tilde{y}_0 \tilde{y}_m} = \mathcal{F}^{-1} \left\{ \mathcal{F} \{ \tilde{y}^{(0)}[n'] \} \cdot (\mathcal{F} \{ \tilde{y}^{(m)}[n'] \})^* \right\} \quad (3)$$

with  $\mathcal{F}$  and  $\mathcal{F}^{-1}$  being the Fast Fourier Transform (FFT) and Inverse Fast Fourier Transform (IFFT) operations, respectively. The estimated phase offset  $\phi^{(m)}$  for the  $m$ th channel relative to the first channel is achieved using the arctangent of the imaginary  $\Im$  and real  $\Re$  parts of the cross correlation function in (3) at the estimated delay  $\hat{\Theta}^{(m)}$  defined as

$$\phi^{(m)} = \text{atan2} \left( \Im \{ R_{\tilde{y}_0 \tilde{y}_m}(\hat{\Theta}^{(m)}) \}, \Re \{ R_{\tilde{y}_0 \tilde{y}_m}(\hat{\Theta}^{(m)}) \} \right) \quad (4)$$

where  $\hat{\Theta}^{(m)} = \arg \max_{\Theta} \{ |R_{\tilde{y}_0 \tilde{y}_m}(\Theta)|^2 \}$  is the delay in samples that maximizes the magnitude of the cross correlation function  $\{|R_{\tilde{y}_0 \tilde{y}_m}(\Theta)|^2\}$ . The estimation process is shown in *RF error calibration* block in Fig. 2. The process is performed over the received signals during ten sections. Thanks to the calibration process, the phase difference between channels is maintained constant over time with a maximum of phase deviation 0.02 degrees proved in [51].

2) *Antenna Calibration*: The use of ideal array steering vector models can cause performance degradation, as already mentioned at the beginning of this work. Misusing antenna array models can lead to significant performance losses in angle estimation techniques [52]. This may result in steering energy toward undesired directions, cancellation of the signal of interest, and amplification of interfering sources [53]. To address these issues and ensure accurate angular measurements, the antenna error calibration process is crucial. However, its accuracy may be affected by environmental changes, limiting its effectiveness in different settings. Therefore, we introduce a calibration process carried out in a

controlled environment, i.e., an anechoic chamber, to minimize reflections and avoid interferences, ensuring more accurate calibration results.

The AoA estimation is performed using a ULA with four elements, spaced at half-wavelength intervals (see Fig. 3). The estimation process evaluates the phase offsets between the receiving antennas. The array is rotated within a defined sector and at specific angular increments. In this work, the range from  $-90^\circ$  to  $90^\circ$ , with a  $5^\circ$  step, covers 37 pilot AoA. The rotary stand (see Fig. 6) is positioned alongside the transmitting antenna at a fixed distance, determined by the tolerable phase deviations, antenna aperture, and wavelength. For the calibration process, a distance of 3 m is used. The transmit power is set to the maximum output value of +18 dBm to ensure a strong received signal, thereby minimizing the impact of instrument noise. This power level is particularly optimal at the carrier frequency of 2.4875 GHz used in this work, but it can vary across different frequencies as specified in [50], as it represents the maximum output power achievable within the experimental parameters. Moreover, a gain setting of 40 dB was selected based on the dynamic range of the USRP NI-2955. This ensures that the received signal remains within its linear operating range, thus avoiding any nonlinearities or compression effects that could negatively impact the signal's amplitude or phase. Note that these adjusters are done according to the specific USRP platform used.

For each angular positions, the bearing errors  $\Delta\phi_i$  are obtained by taking the difference between the estimated value  $\hat{\phi}_i$  and the setting of the rotary stand  $\phi_{\text{pos}_i}$ , i.e.,  $\Delta\phi_i = \phi_{\text{pos}_i} - \hat{\phi}_i$ . The received data stream is then evaluated and compensated for phase offsets induced by free-space propagation. The phase offset  $\phi$  is computed as  $\phi = 2\pi d f_c / c$ , where  $d$  is the distance between antenna elements,  $f_c$  is the carrier frequency, and  $c$  is the speed of light. Spline interpolation is used to facilitate a dense calibration grid, and the calibrated array manifold  $\hat{\mathbf{a}}(\phi)$  is employed to correct array errors in searching-based AoA estimation algorithms. The calibrated array manifold for each angular position is

$$\hat{\mathbf{a}}(\phi) = \text{diag}(\zeta_\phi) \mathbf{a}(\phi). \quad (5)$$

Here,  $\zeta_\phi = [1, e^{j\hat{\phi}_2}, \dots, e^{j\hat{\phi}_N}]$  captures the mismatch array error correction derived from the calibration process,  $\text{diag}$  returns a square diagonal matrix with the vector elements  $\zeta_\phi$  on the main diagonal, and  $\mathbf{a}(\phi) = [1, e^{-j2\pi d \sin(\phi)/\lambda}, \dots, e^{-j2\pi(N-1)d \sin(\phi)/\lambda}]$  represents the theoretical antenna response. Finally, the AoAs are determined by identifying dominant spectral peaks to be explained in Section III-E. The calibration of antennas is performed after the demodulation of OFDM signal (see *AoA estimation* block in Fig. 2). The results of the calibration technique for this work are illustrated in Fig. 7. In this figure, the theoretical array response for each incident direction is compared with the experimental array response, highlighting the computed phase error deviation from the expected value. This deviation is critical for correcting phase errors that originate from the antennas. Although the calibration measurements do not provide an explicit formulation of the array's response as a function of wave-field parameters, applying proper calibration and error correction techniques significantly

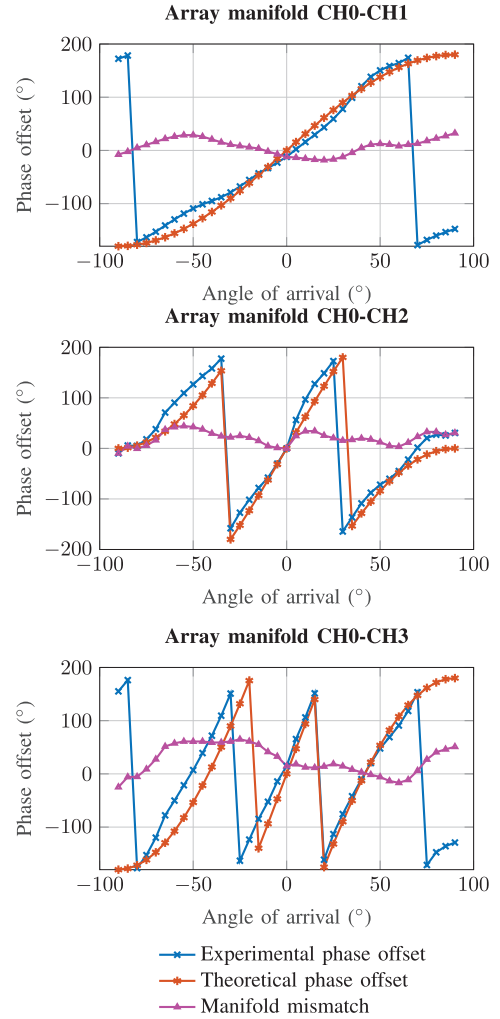


Fig. 7. Estimation of antenna phase errors between the receiving antennas of a ULA array through anechoic chamber-based calibration. The array is rotated within a defined sector ranging from  $-90^\circ$  to  $90^\circ$  in increments of  $5^\circ$ .

improves array processing methods. This, in turn, enhances the performance of high-resolution direction-finding algorithms.

### C. Synchronization

Addressing synchronization errors in OFDM systems is critical, as such errors can disrupt subcarrier orthogonality and significantly degrade system performance. Factors, such as Doppler shifts, oscillator frequency mismatches, and timing inconsistencies, can compromise this orthogonality. Timing offset may lead to intercarrier interference, reducing signal quality and integrity. Similarly, carrier frequency offsets introduce interference from adjacent subcarriers, further disrupting orthogonality. This section will cover the estimation and compensation of symbol time and frequency offsets, as well as frame synchronization, all applied after RF channel calibration (refer to the *time and frequency Synchronization* and *Frame Synchronization* blocks in Fig. 2). The processes for estimating and correcting these offsets are discussed in Section III-C1, followed by frame synchronization in Section III-C2. These processes use a local replica of the known transmitted signal that will be cross-correlated with the actual received signal. Note that, in the context of cellular 5G NR, such synchronization often involves correlating

the received signal with predefined reference signals, such as the primary synchronization signal (PSS) and secondary synchronization signal (SSS) [48], whose structure, sequence, and periodicity are known beforehand by both the transmitter and the receiver. Failure to address synchronization issues can result in improper OFDM demodulation and degraded AoA estimation due to accumulated offsets.

1) *Symbol Timing and Frequency Offset Estimation:* The process involves checking the baseband I/Q samples to estimate and establish time and frequency synchronization of the uplink received signal with the local replica signal  $s_c$  as a reference (see *Time and frequency synchronization* block in Fig. 2). It consists of a two-step process for both time and frequency offset: a coarse estimate carried out in the time domain, and a fine estimate to refine the initial estimates and increase precision. The process is repeated for each of the received RF channels. The  $\tau$ , and Carrier Frequency Offset (CFO) to be considered for compensation to each of the received waveforms will be the mean value. This process synchronizes the received data streams at each of the RF channels to the beginning of the OFDM symbol.

The coarse estimation of CFO is performed by identifying the strongest correlation peak between the received waveform and the local replica of the signal. The CFO  $\varepsilon$  is estimated by searching a frequency range of residual carrier frequency, i.e., from  $-\Delta f$  to  $\Delta f$  with a step size of one-thousandth of  $\Delta f$ , with  $\Delta f$  being the subcarrier spacing. For each frequency in the search range, compensation on the received signal is applied using the equation

$$\hat{y}^{(i)}[n] = y^{(i)}[n] e^{-\frac{j2\pi n \varepsilon}{N}}. \quad (6)$$

Afterward, a correlation between the corrected received signal  $\hat{y}[n]$  and a shifted and conjugated version of the reference signal  $s_c$  is computed, whose correlation's result is

$$R_{ys}(l_\tau) = \sum_{n=0}^{N+N_{cp}-1} \hat{y}^{(i)}[n] s_c^*[n - l_\tau] \quad (7)$$

where  $s_c[n - l_\tau]$  is a circular shift of the local replica waveform resulting in a matched filter of the OFDM signal and  $n$  is the discrete-time in samples. The process is repeated for each set of frequencies in the search range. The estimated time offset is determined by the position of the correlation peak, and the frequency offset is selected as the one that gives the strongest correlation value. The estimated delay is

$$\hat{l}_\tau = \arg \max_{l_\tau} \{|R_{ys}(l_\tau)|^2\}. \quad (8)$$

The fine estimation of time and frequency offset is done by performing a data interpolation around the coarse estimation value. Note that the accuracy of the carrier frequency offset estimation is limited to the subcarrier spacing. Finally, the corrected received stream at  $i$ th RF channel has the form

$$\hat{y}^{(i)}[n] = \mathbf{y}^{(i)}[n + \hat{l}_\tau^{(\text{fine})}] e^{-\frac{j2\pi n \varepsilon^{(\text{fine})}}{N}} + w^{(i)}[n]. \quad (9)$$

2) *Frame Synchronization:* The time offset estimated in III-C1 aligns only with the start of the OFDM symbol. To obtain the start of the frame, frame synchronization is undertaken. This process, which is crucial during the demodulation process of the 5G NR signal, is depicted in Fig. 8.

During transmission, the symbols are sent through the channel using parallel-to-serial conversion, and upon reception, symbol samples arrive sequentially. Since OFDM operates in frames, the receiver needs to gather a set of OFDM symbols to demodulate. To accurately detect the start of frames, the previously estimated time and frequency offset are removed from the received signal as in (9), and the result is correlated in time with the locally generated frame similar to (7). The pilot signals from the replica are used as markers. These pilot signals have unique correlation properties in the time domain, allowing the receiver to detect frame beginnings accurately. The cross correlation generates prominent peaks that serve as indicators to estimate the starting position of the frame, which dictates the alignment of the FFT window in the receiver with the useful part of the OFDM symbol. Depending on the estimated time offset, two scenarios are possible.

- 1) *Case 1:* When the time offset is positive and the local replica is placed earlier than the received stream, the frame is situated  $\Theta_\tau$  samples after the beginning of the received stream.
- 2) *Case 2:* When the estimated time offset is negative, meaning the received signal arrived earlier at the RF channel compared to the local replica, the first  $\Theta_\tau$  samples of the frame are discarded to align with the beginning of the frame.

The corrected received stream at  $i$ th RF channel is

$$\mathbf{y}_{FR}^{(i)}[n] = \hat{\mathbf{y}}^{(i)}[n + \Theta_\tau]. \quad (10)$$

Note that the synchronization process is applied after the RF channel error calibration process (see Fig. 2) to be explained in Section III-B1.

#### D. Signal Demodulation and Extraction

The signal demodulation and extraction module captures the compensated waveforms at each of the radio channels (refer to the *Signal demodulation and extraction* block in Fig. 2) and performs the demodulation process. First, the time-domain multichannel SRS signals are transformed into the frequency domain using FFT, and the CP from each OFDM symbol is removed. The resulting received signal after demodulation, at the  $k$ th symbol and  $m$ th subcarrier, is given by the equation

$$Y'(k, m) = H(k, m)b(k, m)e^{j\theta_{\text{offset}}(k, m)} + w(k, m) \quad (11)$$

where  $H(k, m)$  is the channel response,  $b(k, m)$  is the complex-valued symbol transmitted,  $\theta_{\text{offset}}(k, m)$  is the residual phase offset at the  $k$ th OFDM symbol and  $m$ th subcarrier, and  $w(k, m)$  is thermal noise, statistically uncorrelated with  $w(k, m) \sim \mathcal{CN}(0, \sigma_w^2)$ .

Despite error corrections, timing errors or synchronization inaccuracies can cause the receiver to sample the signal at slightly different instants than intended, leading to a perceived frequency offset known as residual CFO. Additional phase offset compensation is performed to ensure reliable data recovery, involving a residual phase offset estimation. The residual carrier offset can vary with the subcarrier due to channel effects, channel delay spread, synchronization errors, and interference. Therefore, phase shift estimation is carried out per subcarrier during the entire reception time. This estimation

necessitates knowledge of the 5G NR uplink signal SRS pattern to collect the received symbols of a frame where SRS pilots are encountered. The received pilots of each subcarrier per OFDM symbols during  $T$  time duration are multiplied with the complex conjugate of the corresponding local replica

$$R(k, m) = Y'(k, m)b^*(k, m) \quad (12)$$

where  $b^*(k, m)$  is the conjugate pilot. The process is repeated for each RF channel receiver. This aligns the subcarriers closely together and retains only the effect of the phase shift, simplifying accurate channel estimation and equalization as the impact of subcarrier spacing is removed. The residual phase offset of first RF channel at the  $m$ th subcarrier is computed as

$$\theta_{\text{offset}}(k, m) = \angle R(k, m). \quad (13)$$

The computed phase offset is applied to the corresponding subcarriers of the rest of the RF channels.

### E. AoA Estimation

The AoA estimation module performs the estimation of angle of arrival using several techniques ranging from classical to modern approaches. These techniques can be categorized into three groups: classical, subspace-based, and parameter-free iterative methods. In the classical AoA techniques, the Delay And Sum (DAS) technique [39] is considered. This method aligns received signals to compensate for propagation delays from different directions to a ULA. By scanning multiple angles and summing the aligned signals, it generates a spatial spectrum, selecting the angle with the highest power as the estimated AoA. While simple, this method has low resolution and is more susceptible to interference and noise. For the subspace AoA techniques, Multiple Signal Classification (MUSIC) [40] and Estimation of Signal Parameters via Rotational Invariance Techniques (ESPRIT) [41] are considered. MUSIC decomposes the covariance matrix of received signals into signal and noise subspaces using eigenvalue decomposition. AoA angles are estimated by finding directions where the steering vector is orthogonal to the noise subspace. This method offers high accuracy but requires prior knowledge of the number of incoming signals. ESPRIT, instead of spectral searching, exploits the rotational invariance of the signal subspace by dividing the antenna array into overlapping subarrays. By analyzing phase shifts between these subarrays, ESPRIT directly estimates the AoAs, reducing the computational complexity to MUSIC. Finally, about the parameter-free iterative AoA techniques, IAA [42], [43] rooted in sparse techniques, series of iterative SAMV approaches [44], [45], [46] based on the asymptotically minimum variance, and SAMV-SML approaches [46] grid-limit free are considered. The IAA is a sparse-based iterative method that continuously reweights received signal data to enhance resolution and robustness, without requiring prior knowledge of the number of sources. SAMV method iteratively refines AoA estimation using sparse recovery techniques, and SAMV-SML further improves performance in scenarios with limited snapshots, ensuring stability in complex environments.

The steering vector for the AoA estimation  $\theta_u$  for each signal  $\mathbf{y}_u$  from the  $u$ th source that impinges on the array (see Fig. 3) is

$$\mathbf{a}_u(\theta) = \left[ 1e^{-j\frac{2\pi}{\lambda} \sin(\theta_u)} e^{-j2\frac{2\pi}{\lambda} \sin(\theta_u)}, \dots, e^{-j\frac{(M-1)\pi}{\lambda} \sin(\theta_u)} \right]^T. \quad (14)$$

The number of sources is estimated using the minimum descriptive length (MDL) method as follows:

$$\text{MDL}(q) = -\log \left( \prod_{j=q+1}^M \lambda_j^{\frac{1}{M-q}} \left( \frac{1}{M-q} \sum_{j=q+1}^M \lambda_j \right)^{M-1} \right) + \frac{1}{2}q(2M-q) \log N \quad (15)$$

where  $q$  is the number of estimated paths,  $M$  is the number of array elements,  $\lambda_j$  are the eigenvalues of the sample covariance matrix of the received signals, and  $N$  is the number of data samples. The number of sources is chosen as the value of  $q$  that minimizes the MDL criterion

$$\hat{q} = \arg \min_q \text{MDL}(q). \quad (16)$$

## IV. SIMULATION ANALYSIS

This section analyzes the key factors affecting AoA estimation accuracy, with a specific focus on the effects of calibration and multipath. The estimation accuracy is influenced by variables such as carrier frequency offset, time offset, and antenna array calibration. In Section IV-A, we analyze the impact of calibration on AoA estimation through simulations conducted in a controlled, multipath-free environment. This study underscores the critical role of synchronization achieved via calibration and its effect on overall estimation precision. Section IV-B transitions to real-world scenarios, where multipath and interference are inevitable. We explore how these factors degrade estimation accuracy and compare the performance of different AoA estimation algorithms under such challenging conditions. For this analysis, we consider the 5G uplink SRS signal, which comprises 4 SRS symbols per slot and is transmitted periodically at a carrier frequency of 2.4875 GHz. A full-band SRS transmission of 25 MHz is used, corresponding to a sampling rate of 30.72 MHz, along with a linear antenna array of four elements. These parameters are consistently applied throughout the article.

### A. Effect of Calibration on AoA Estimation

Monte Carlo simulations were conducted to evaluate the statistical behavior of frequency and time offset error estimation, focusing on the impact of residual synchronization errors on AoA accuracy. The analysis explores how these residual errors influence estimation performance across different SNR levels. Phase offsets introduced by the front-end hardware are specified as follows:  $\Phi'_{\text{Ch0-Ch1}} = \pi/3$ ,  $\Phi'_{\text{Ch0-Ch2}} = \pi/4$ , and  $\Phi'_{\text{Ch0-Ch3}} = \pi/6$ . The carrier offset is varied from 3 to 4.5 kHz in steps of 0.25 kHz, and a time offset of 0.97 ns is applied to the waveform. The true AoA for estimation is set at 22 degrees. For each combination of carrier offset and SNR (ranging from

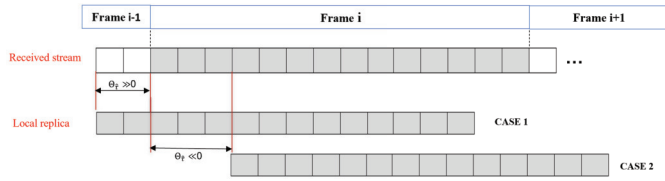


Fig. 8. Frame synchronization process to precisely align the start of a 5G NR frame.

–10 to 25 dB in 5 dB increments), 30 realizations are generated, and frequency, time, and AoA estimations are performed. The chosen range of carrier frequency offset corresponds to one-tenth of the subcarrier spacing, reflecting a step size of 1.5 kHz, and is selected to evaluate the fine accuracy of the AoA estimation process. The results are compared with the Cramér-Rao Bound (CRB) values. The Cramér-Rao bound (CRB) for delay offset estimation is derived using the general assumptions from [54] and [55], and it is expressed as

$$\text{CRB}(\hat{\tau}) = \frac{6}{\text{SNR} \cdot N_{\text{ant}} \cdot N_{\text{OFDM}} \cdot N_a (N_a^2 - 1)} \cdot \frac{1}{(2\pi\Delta f K_{\text{TC}})^2} \quad (17)$$

where SNR is the average SNR per resource element,  $N_{\text{ant}}$  is the number of the antenna elements in the array,  $N_{\text{OFDM}}$  is the number of OFDM SRS symbols considered,  $N_a$  is the total number of active pilot subcarriers, and  $K_{\text{TC}}$  is the transmission comb number, representing the minimum frequency separation between two subcarriers allocated for SRS. Consequently, the CRB for range estimation can be expressed as  $\text{CRB}(R_r) = c^2\text{CRB}(\hat{\tau})$ , where  $c$  is the speed of light. The CRB for CFO estimation according to the derivations in [56] is

$$\text{CRB}(\hat{\epsilon}) = \frac{(1 - \rho^2)}{8\pi\rho^2L} \quad (18)$$

where  $\rho = (\sigma_b^2/(\sigma_b^2 + \sigma_w^2))$  is derived from  $\rho = (\text{SNR}/(\text{SNR} + 1))$ , with  $\text{SNR} = (\sigma_b^2/\sigma_w^2)$  representing the average SNR per resource element and  $L$  is the length of the cyclic prefix. As CFO estimation includes the cyclic prefix, increasing its length can make the CRB arbitrarily small. Finally, the CRB of AoA estimation, assuming a LoS channel, derived based on the configurations presented in [55], is

$$\text{CRB}(\hat{\theta}) = \frac{6}{\text{SNR} \cdot N_{\text{ant}} \cdot N_a \left(\frac{w_c d}{c}\right)^2 (N_{\text{ant}}^2 - 1) \sin^2 \theta} \quad (19)$$

where  $w_c = 2\pi f_c$  is the angular frequency, with  $f_c$  as the carrier frequency. Increasing the number of antenna elements further reduces angle estimation errors.

The results, shown in Fig. 9, illustrate the root-mean-square error (RMSE) of frequency offset estimation as a function of SNR. The method demonstrates high accuracy in identifying the central maxima corresponding to the target frequency offset, with estimation errors below 5 Hz for SNR above 0 dB. However, at lower SNR, the error increases to over 10 Hz. For intermediate SNR values, estimation accuracy degrades gradually, with an error of approximately 1 Hz at high SNR and up to 6 Hz at low SNR. The results indicate a clear improvement in frequency offset estimation

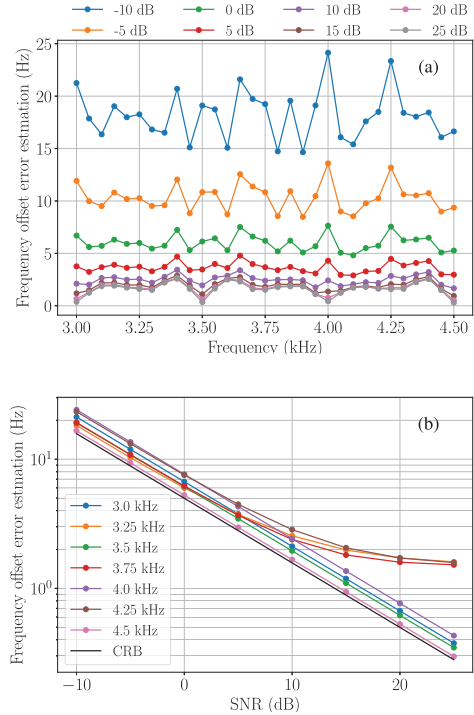


Fig. 9. Evaluating the accuracy of carrier frequency offset estimation. The carrier offset is varied from 3 to 4.5 kHz in steps of 0.25 kHz. In (a) it is presented the frequency offset error for different carrier frequency offsets and in (b) frequency offset error depending on SNR values.

as SNR increases. Specifically, for frequency offsets with a resolution of 1.5 kHz, the Root-Mean-Square Error (RMSE) error stabilizes at around 1.5 Hz for SNR values above 20 dB, showing minimal change with further increases in SNR. This is because the offsets are near the central maxima of the frequency estimation function, and the algorithm struggles to distinguish between closely spaced frequencies. Therefore, for better results, the frequency resolution should ideally be within the range of a few Hz. In this study, a frequency resolution of 10 Hz was used, which meets the accuracy requirements for the given experimental conditions. Note that, in practical applications, frequency resolution may vary due to several factors, particularly the quality of the hardware and its clock. Consequently, the use of a high-quality clock or an external clock may require adjustments to the frequency resolution to meet specific operational needs.

In contrast, time offset estimation accuracy, reflected in range delay and angle resolution, is presented in Fig. 10. The accuracy of the carrier frequency offset influences these results as well. The analysis shows that both time and angle offset estimation accuracy improve at higher SNR levels. Thus, under conditions of perfect antenna calibration and precise RF channel error estimation, even with frequency offset errors up to 25 Hz and a single source, the algorithms can achieve an angle of arrival resolution of less than 1 degree.

### B. Effect of Multipath on AoA Estimation

Many angle-dependent algorithms [39], [40], [41] struggle when dealing with coherent sources, as previously outlined in the introduction, due to rank deficiencies in the source

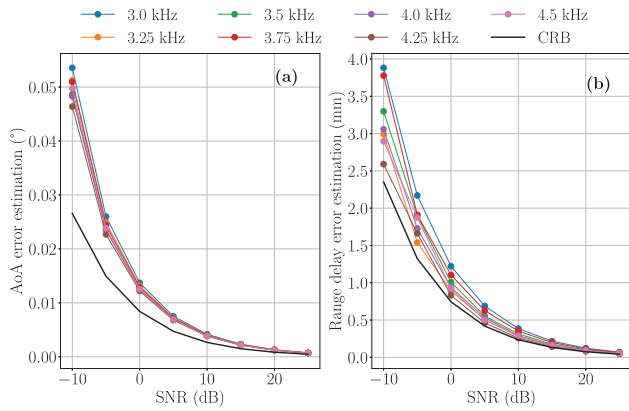


Fig. 10. Evaluating the accuracy of time offset and angle of arrival estimation. In (a) it is presented the angle error estimation versus SNR values and in (b) range delay error estimation versus SNR values.

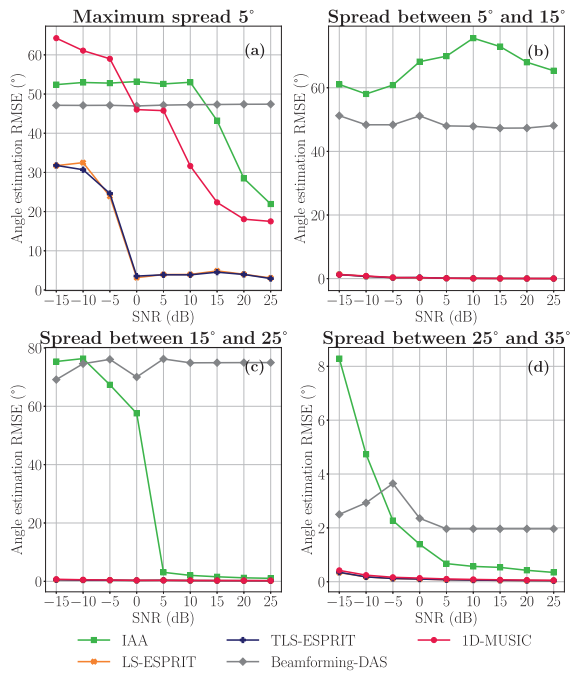


Fig. 11. Angle estimation error for different angle spreads using classic techniques. (a) Spread below  $5^\circ$ , (b) spread between  $5^\circ$  and  $15^\circ$ , (c) spread between  $15^\circ$  and  $25^\circ$ , and (d) spread between  $25^\circ$  and  $35^\circ$ .

covariance matrix and the requirement for more antenna elements than the number of incoming signals. This section evaluates the performance of the algorithms from Section III-E in multipath and coherent signal environments. The analysis is based on 50 Monte Carlo trials for each SNR value, ranging from  $-15$  to  $25$  dB in 5 dB increments. Two coherent sources are considered: one fixed at  $0^\circ$  with no time delay, and another with varying angles and delays across short to long ranges. The angle spread is set to  $35^\circ$ , covering a sector centered on the reference direction, with possible angles from  $-35^\circ$  to  $+35^\circ$ . Both sources share identical waveforms, and 63 snapshots are captured per estimation. Results are categorized by angle spread into very short, short, and long directions, as shown in Figs. 11 and 12. The very short group has a maximum spread of  $5^\circ$  ( $-5^\circ$  to  $5^\circ$ ), the short group spans  $5^\circ$  to  $15^\circ$ , the next covers  $15^\circ$  to  $25^\circ$ , and the longest extends from  $25^\circ$  to  $35^\circ$ . Additionally, multipath signals are assigned a random delay

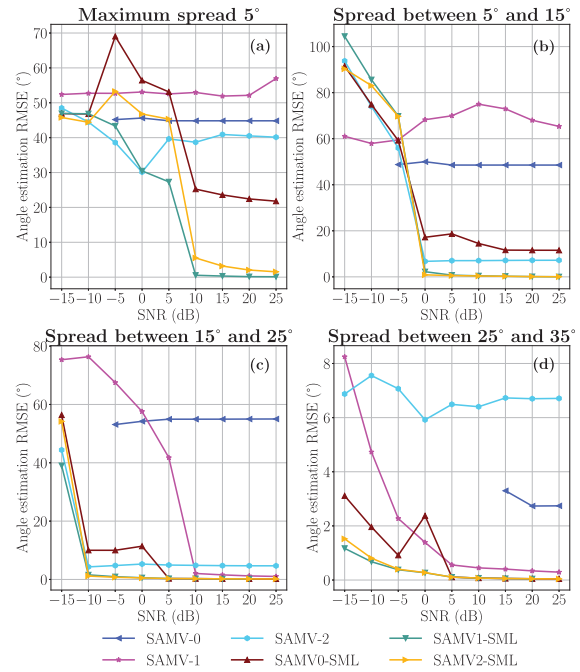


Fig. 12. Angle estimation error for different angle spreads using sparse asymptotic minimum variance approaches: (a) spread below  $5^\circ$ , (b) spread between  $5^\circ$  and  $15^\circ$ , (c) spread between  $15^\circ$  and  $25^\circ$ , and (d) spread between  $25^\circ$  and  $35^\circ$ .

spread of 1, 2, or 3 samples (i.e., 32.55, 65.10, and 97.65 ns, respectively). For subspace- and power-based methods, a scanning grid with a  $0.2^\circ$  step size covers the  $-90^\circ$  to  $90^\circ$  range. Iterative approaches perform up to 60 iterations per estimation.

The results indicate that due to smearing effects and limited resolution, both MUSIC and classical beamforming struggle to separate closely spaced sources. Eigen-analysis-based MUSIC and 2-D beamforming fail to distinguish between coherent signals. However, simulations show that treating spatial and temporal dimensions independently—resolving one at a time—enables separation due to super-resolution capabilities. Signals arriving at different angles create distinct spatial patterns influenced by time delays. Angular estimation improves significantly when sources are separated by more than  $5^\circ$  and have a time delay exceeding one sample. For closely spaced sources, the angular estimation error decreases at high SNR. The total least squares (TLSs) ESPRIT method performs slightly better than least squares (LSs) ESPRIT, though their accuracy differences diminish at higher SNR and wider angle spreads. Both outperform other spatial-based techniques, halving the angle error for closely placed sources. When delay spreads increase, spatial-based methods achieve estimation errors below  $2^\circ$ . Beamforming performs worse, particularly at larger angular spreads. Due to its data-independent nature and fewer antenna elements, classical beamforming (DAS) has lower resolution, wider main lobes, and reduced angular precision, limiting its ability to distinguish signals. The achieved accuracy remains within  $2^\circ$ .

Power-based techniques provide higher-resolution spatial estimates, reducing smearing effects, but fail to separate closely spaced sources at low SNR. Sparse methods like SAMV and SAMV-SML outperform IAA due to differences

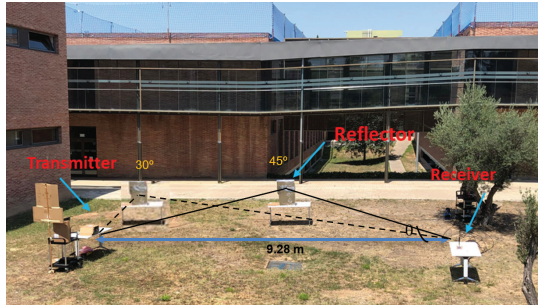
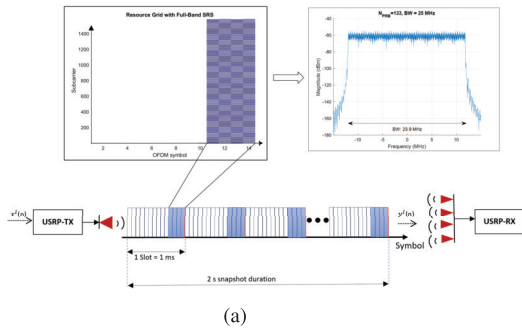


Fig. 13. Outdoor experiment details: in (a) structure of the signal is presented, in (b) picture of the experimental setup is shown.

in power matrix estimation. IAA sums signal magnitudes, causing covariance matrix singularity, while SAMV computes power estimates iteratively: SAMV-0 uses previous estimates, SAMV-1 incorporates Capon power, and SAMV-2 combines both. At SNR >5 dB and with more snapshots, IAA improves, but SAMV-2 achieves superior resolution. Sparse techniques are limited by the direction scanning grid, whereas grid-free SAMV-SML provides the highest accuracy (<1°) and is more robust to insufficient snapshots. SAMV-0 performs poorly at low SNR, while SAMV-2 reduces angle estimation errors to <20° even for closely spaced sources. At larger angle spreads and higher SNR, SAMV-1 performs similarly to SAMV-2 and IAA.

### V. EXPERIMENTAL ANALYSIS

To assess the effectiveness of the suggested receiver and verify the feasibility of calibrating angle estimation accuracy, outdoor experiments are conducted. These experiments took place in an open area in the backyard of the Autonomous University of Barcelona, Spain. This section will first present the experimental setup, followed by an analysis of the results, which evaluates the impact of calibration and environmental conditions such as multipath and interference. The number of incoming signals is estimated using the Minimum Descriptive Length (MDL) criterion.

#### A. Experimental Setup

Two different setups are employed for the outdoor experiment: one with no multipath, and one in the presence of multipath. For the first setup with no multipath, where the transmitter and receiver are in LoS conditions, the linear array composed of four elements at the receiver side is swiveled to

obtain different angles of arrival (from -60° to 60° with a step size of 10°). For the second setup, a reflector is placed in two different positions as depicted in Fig. 13(b): the reflector placed between the transmitter and receiver, creating a 45° AoA; and the reflector positioned near the transmitter at a distance of 4 m, creating a 30° AoA. Here, the transmitter’s AoA is fixed at 0°, and only the reflector is moved to form the desired angles. The reflector body, with dimensions of 112 cm (length) × 50 cm (width) × 45.5 cm (height), is constructed from aluminum foil, with a thickness of approximately ±0.6 mm. Aluminum foil is effective as a reflective material due to its ability to minimize penetration and maximize energy reflection as outlined in [57]. It can achieve reflectivity levels of up to 93.3%. In both scenarios, the transmitter and receiver are placed within a distance of 9.28 m. The distance is limited to the use of industrial, scientific and medical (ISM) band (i.e., a carrier frequency of 2.4875 GHz), and its inherent power limitations. The increase in the distance can lead to signal and potentially introduce line of sight (NLoS) NLoS effects, such as signal fading and increased noise levels, which could significantly impact the accuracy and reliability of the measurements. The SRS signal is transmitted periodically every 1 ms for 2 s from the single antenna port of the transmitter [see Fig. 13(a)]. Recall that the USRP N310 is used as a transmitter and as a receiver, the USRP NI2955. The system parameters used include a transmission gain of 65 dB, and a sampling rate of 30.72 Msps, which corresponds to a 25 MHz bandwidth. The full band is used for the transmission. Omnidirectional monopole antennas are used for both transmission (TX) and reception (RX). The single transmitter antenna is mounted directly on one of the transmission channels of the TX-N310. On the receiver’s side, the antennas are mounted on a platform with a separation of λ/2 between the elements of the antenna to enhance resolution ability in the presence of interference. To mitigate interference, only interference-free subcarriers are selected after waveform demodulation, leveraging the inherent properties of OFDM. In this work, the interference, detected at a center frequency of 2.479 GHz with a 2 MHz bandwidth, is addressed through this correction strategy. The samples are recorded using LabVIEW. For each scenario (i.e., reflector at 30° and at 45°), 3 tests are conducted, each corresponding to an independent data stream capture (i.e., snapshot). Each snapshot is recorded for 2 s, followed by a 1-minute interval between capturing the next one. Throughout the process, the experimental setup remains unchanged, with no modification to the configuration parameters of the physical arrangement. For this experiment, we estimate the AoA from signal reflections to evaluate the system’s ability to detect Non Line of Sight (NLoS) paths.

This study focuses on azimuth angle estimation, as the transmitter and receiver are on the same horizontal plane. The dipole antenna array’s omnidirectional radiation in azimuth but minimal gain in elevation makes vertical propagation negligible. Additionally, the ULA is sensitive to azimuth angles. Since elevation variations have little impact on accuracy, they are not considered. Incorporating elevation would require tiltable antennas, a 3-D positioning system, and updates to the steering vector and estimation algorithms.

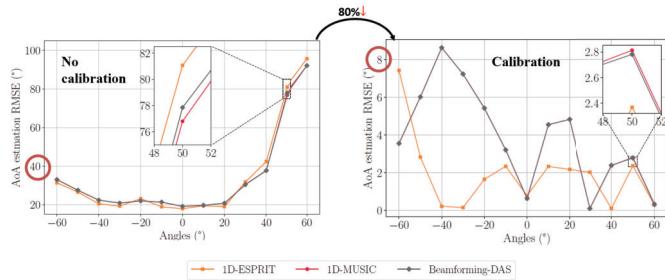


Fig. 14. RMSE angle estimation under LoS conditions: (left) without calibration, and (right) with calibration.

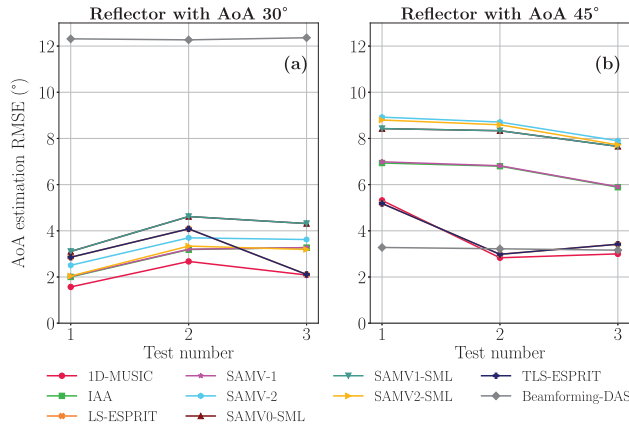


Fig. 15. Multipath environment: angle of arrival estimation accuracy of the reflector body. In (a) reflector is placed at  $30^\circ$ , in (b) at  $45^\circ$ .

## B. Experimental Results

1) *AoA Estimation in Multipath Free Environment*: This section evaluates the performance of the proposed receiver in a nonmultipath scenario using conventional subspace-based techniques such as MUSIC and ESPRIT, as well as classical beamforming to perform the angular estimation. The results shown in Fig. 14 indicate that implementing calibration reduces angle estimation error by fourfold, demonstrating the significant impact of calibration on angle measurements. Additionally, the results show that the angle estimation error decreases as the angle approaches  $0^\circ$ , but increases near the endfire position of the antenna array. Moreover, taking into account that the phase deviation concerning a planar wave increases toward the edge of the antenna, at the carrier frequency of 2.4875 GHz, there is an additional  $1.3^\circ$  of phase deviation present. Both MUSIC and beamforming demonstrate similar performance in terms of estimation accuracy for all angles, with MUSIC achieving a slightly lower error estimation of  $0.05^\circ$ . The method yields a maximum angle error estimation of approximately  $8.6^\circ$  and a minimum of approximately  $0.1^\circ$ , with an average error estimation of around  $\sim 3.8^\circ$ . Both methods consistently estimate all considered snapshots, with a standard deviation of approximately  $\sim 2.6^\circ$ .

2) *AoA Estimation in Multipath Environment*: This section evaluates the accuracy of angle estimation in the presence of multipath. The results are obtained by three tests, each corresponding to different captured data streams while maintaining the same conditions as depicted in Fig. 15. Based on the MDL approach, the number of incoming signals is 3. However, it is important to note that this method might incorrectly estimate

the number of incoming signals, leading to the appearance of false angular estimates. When considering 3 incoming signals for a four-element array, the MUSIC reduces to the Pisarenko method, where the angle is estimated as the angular position of the roots, omitting the problem of separating the “signal roots” from the “noise roots”. Despite its computational simplicity, the Pisarenko method may have relatively poor statistical accuracy. However, in our specific case, it can effectively distinguish the presence of the expected signals from different paths as observed from the results obtained in Section IV-B.

For the case of reflection with an AoA  $30^\circ$ , the results show high performance, with the AoA estimation accuracy being below  $4^\circ$  for all considered techniques, except for beamforming, which shows higher error estimation. Beamforming performance depends on the main lobe width and its ability to distinguish sources at different angles. With only four elements, the ULA has a relatively wide main lobe, limiting resolution. At  $30^\circ$ , secondary lobes shift the reflection peak, reducing accuracy. In contrast, at  $45^\circ$ , the larger angular separation minimizes these effects, improving detection. The lowest angle error is achieved by the MUSIC method with an error below  $1.5^\circ$ . IAA, SAMV-1, and SAMV2-SML give similar resolution with an angle error  $< 3^\circ$ . SAMV0-SML and SAMV1-SML all demonstrate similar resolution, with an angle error below  $3^\circ$ . Apart from beamforming, the 1-D estimation of ESPRIT (both the Least Squares (LS) and the Total Least Squares (TLS) approach) gives the worst estimation with a maximum angle error of  $3.9^\circ$ .

In the case of a reflection with an AoA  $45^\circ$ , the maximum angle error estimation computed is  $8.9^\circ$ . Even in this case, the MUSIC method presents a better resolution in the last two tests. The performance of beamforming has improved, with an averaged angle error of approximately  $4^\circ$ . IAA and SAMV-1 yield very similar results with an error estimation of  $6.47^\circ$  on average. The SAMV-SML techniques produce the highest estimation error compared to the other methods, as the output of SAMV-2 is used as input to the algorithm, and the results indicate that these methods have the worst performance.

Overall, the estimation for the second case is worse than for the first case. This can be attributed to the use of aluminum foil to build the reflection body, which possesses different diffuse properties based on its bright and matte sides. Although the bright side was chosen, the scatter of the arriving signal also depends on the signal direction, with some angles exhibiting more scatter than others, as outlined in [58], [59], and [60]. These limitations, along with some residuals remaining during the calibration phase, have contributed to the degradation of the results.

3) *Impact of Calibration in AoA Estimation*: It is important to assess the impact of calibration on AoA estimation to determine whether both the calibration of the RF channel error and antenna error have equal contributions to the accuracy of the estimation. The angle estimation data obtained during antenna calibration in the anechoic chamber reveals that the array error is negligible, except when the array is in the endfire position, known for its poor performance. The results shown in Fig. 16 indicate that the effect of antenna calibration on error correction is minimal compared to the contribution of RF

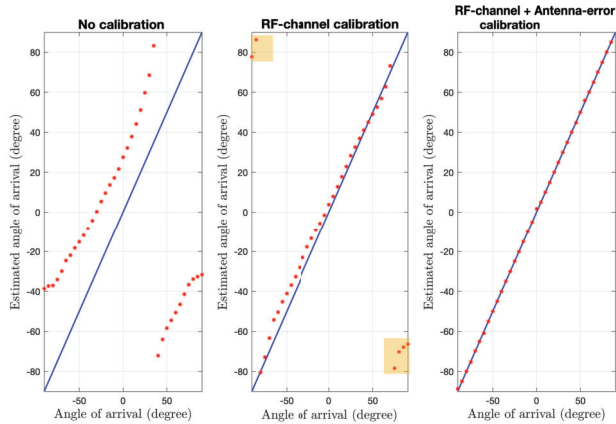


Fig. 16. Impact of antenna calibration on angle estimation: (left) without calibration, (middle) with RF-channel calibration, and (right) with both RF-channel and antenna error calibration.

channel error calibration. For scenarios where high accuracy is not crucial, calibration only on the RF channels side is sufficient. However, for better performance, both calibration contributions should be taken into account.

## VI. CONCLUSION

In this work, we have proposed an efficient receiver to calibrate angle error measurements, investigate the array modeling, and provide accurate AoA estimates using 5G NR signals. The receiver consists of several steps, such as data processing (signal extraction), calibration (RF channel error calibration and antenna error calibration), and synchronization (a time delay and frequency offset estimation, and frame synchronization) to finally provide the AoA estimation. The results showcase a significant improvement in AoA estimation accuracy compared to the case without calibration, particularly in the presence of multipath and interference. Overall, the angle estimation obtained following our proposed end-to-end system appears to be very accurate. When no multipath is presented, a maximum of  $\sim 8.6^\circ$  and a minimum of  $\sim 0.1^\circ$  angle error estimation is achieved using conventional methods. The average error estimation is  $\sim 3.8^\circ$ . The methods are consistent in their estimation of all considered snapshots with a standard deviation of  $\sim 2.6^\circ$ . In the presence of multipath, when using conventional methods, the lowest angle error obtained is below  $2^\circ$ , and the highest angle error is  $12.3^\circ$ . To improve the angle estimation, we explored more modern and complex AoA estimation algorithms. The lowest angle error achieved is below  $2^\circ$ , and the highest is below  $8.9^\circ$ . Both methods, conventional and unconventional, showcase a scalable solution for real-world applications, underscoring the practical impact of the research. Finally, a significant improvement in AoA estimation accuracy was achieved with calibration, where RF channel error calibration was shown to have a greater impact compared to antenna calibration.

To mitigate multipath interference, strategies like elevating the antennas, avoiding metal-framed desks, or using foam pyramid absorbers can be applied. Despite these challenges, calibration effectively minimized errors, especially for primary angles facing the transmitter. Angle estimation accuracy varies

due to antenna directionality, nonuniform gain, and environmental factors such as multipath from tall trees and metal structures, emphasizing the importance of calibration to reduce these effects.

## REFERENCES

- [1] Y. Ruan, L. Chen, X. Zhou, G. Guo, and R. Chen, "Hi-Loc: Hybrid indoor localization via enhanced 5G NR CSI," *IEEE Trans. Instrum. Meas.*, vol. 71, pp. 1–15, 2022.
- [2] J. Nikonowicz, A. Mahmood, M. I. Ashraf, E. Björnson, and M. Gidlund, "Indoor positioning in 5G-advanced: Challenges and solution towards centimeter-level accuracy with carrier phase enhancements," 2022, *arXiv:2209.01183*.
- [3] S. Hakak et al., "Autonomous vehicles in 5G and beyond: A survey," *Veh. Commun.*, vol. 39, p. 100551, Feb. 2023.
- [4] J. Ahlander and M. Posluk, "Deployment strategies for high accuracy and availability indoor positioning with 5G," Ph.D. dissertation, Dept. Elect. Eng., Autom. Control, Linköping Univ., 2020.
- [5] A. Fouda, R. Keating, and H.-S. Cha, "Toward cm-level accuracy: Carrier phase positioning for IIoT in 5G-advanced NR networks," in *Proc. IEEE 33rd Annu. Int. Symp. Pers., Indoor Mobile Radio Commun. (PIMRC)*, Sep. 2022, pp. 782–787.
- [6] A. Behravan et al., "Positioning and sensing in 6G: Gaps, challenges, and opportunities," *IEEE Veh. Technol. Mag.*, vol. 18, no. 1, pp. 40–48, Mar. 2023.
- [7] X. Lin and N. Lee, *5G and Beyond*. Cham, Switzerland: Springer, 2021.
- [8] M. Shafi et al., "5G: A tutorial overview of standards, trials, challenges, deployment, and practice," *IEEE J. Sel. Areas Commun.*, vol. 35, no. 6, pp. 1201–1221, Jun. 2017.
- [9] F. Campolo, A. Blaga, M. Rea, A. Lozano, and X. Costa-Pérez, "5GNSS: Fusion of 5G-NR and GNSS localization for enhanced positioning accuracy and reliability," *IEEE Trans. Veh. Technol.*, vol. 73, no. 9, pp. 13558–13568, Sep. 2024.
- [10] A. Conti et al., "Location awareness in beyond 5G networks," *IEEE Commun. Mag.*, vol. 59, no. 11, pp. 22–27, Nov. 2021.
- [11] A. Yassin et al., "Recent advances in indoor localization: A survey on theoretical approaches and applications," *IEEE Commun. Surveys Tuts.*, vol. 19, no. 2, pp. 1327–1346, 2nd Quart., 2016.
- [12] Z. Li, Z. Tian, and M. Zhou, "Decimeter level indoor localization using hybrid measurements of a distributed single receiver," *IEEE Trans. Instrum. Meas.*, vol. 70, pp. 1–14, 2021.
- [13] A. Xhafa, J. A. del Peral-Rosado, J. A. López-Salcedo, and G. Seco-Granados, "Evaluation of 5G positioning performance based on UTD0A, AoA and base-station selective exclusion," *Sensors*, vol. 22, no. 1, p. 101, 2021.
- [14] Z. Abu-Shaban, X. Zhou, T. Abhayapala, G. Seco-Granados, and H. Wymeersch, "Error bounds for uplink and downlink 3D localization in 5G millimeter wave systems," *IEEE Trans. Wireless Commun.*, vol. 17, no. 8, pp. 4939–4954, Aug. 2018.
- [15] W. Roh et al., "Millimeter-wave beamforming as an enabling technology for 5G cellular communications: Theoretical feasibility and prototype results," *IEEE Commun. Mag.*, vol. 52, no. 2, pp. 106–113, Feb. 2014.
- [16] B. Amjad, Q. Z. Ahmed, P. I. Lazaridis, F. A. Khan, M. Hafeez, and Z. D. Zaharis, "Deep learning approach for optimal localization using an mm-wave sensor," *IEEE Trans. Instrum. Meas.*, vol. 72, pp. 1–15, 2023.
- [17] H. Chen, H. Sarrideen, T. Ballal, H. Wymeersch, M. Alouini, and T. Y. Al-Naffouri, "A tutorial on terahertz-band localization for 6G communication systems," *IEEE Commun. Surveys Tuts.*, vol. 24, no. 3, pp. 1780–1815, 3rd Quart., 2022.
- [18] H. Sarrideen, M.-S. Alouini, and T. Y. Al-Naffouri, "An overview of signal processing techniques for terahertz communications," *Proc. IEEE*, vol. 109, no. 10, pp. 1628–1665, Oct. 2021.
- [19] S. Fischer, "5g nr positioning," in *5G and Beyond: Fundamentals and Standards*. Cham, Switzerland: Springer, 2021, pp. 429–483.
- [20] *Study NR Positioning Enhancements*, Standard TR38.857, Rel. 17, 3GPP, Mar. 2021.
- [21] S. Ahmadi, *5G NR: Architecture, Technology, Implementation, and Operation of 3GPP New Radio Standards*. New York, NY, USA: Academic, 2019.
- [22] B. Sun, B. Tan, W. Wang, and E. S. Lohan, "A comparative study of 3D UE positioning in 5G new radio with a single station," *Sensors*, vol. 21, no. 4, p. 1178, Feb. 2021.

- [23] M. A. Nazari, G. Seco-Granados, P. Johansson, and H. Wymeersch, "mmWave 6D radio localization with a snapshot observation from a single bs," *IEEE Trans. Veh. Technol.*, vol. 72, no. 7, pp. 8914–8928, 2023.
- [24] A. Blanco, N. Ludant, P. J. Mateo, Z. Shi, Y. Wang, and J. Widmer, "Performance evaluation of single base station ToA-AoA localization in an LTE testbed," in *Proc. IEEE 30th Annu. Int. Symp. Pers., Indoor Mobile Radio Commun. (PIMRC)*, Sep. 2019, pp. 1–6.
- [25] F. Morselli, S. M. Razavi, M. Z. Win, and A. Conti, "Soft information-based localization for 5G networks and beyond," *IEEE Trans. Wireless Commun.*, vol. 22, no. 12, pp. 9923–9938, Dec. 2023.
- [26] G. Fokin, "AOA measurement processing for positioning using unmanned aerial vehicles," in *Proc. IEEE Int. Black Sea Conf. Commun. Netw. (BlackSeaCom)*, Jun. 2019, pp. 1–3.
- [27] J. Cheng, K. Guan, and F. Quitin, "Direction-of-arrival estimation with virtual antenna array: Observability analysis, local oscillator frequency offset compensation, and experimental results," *IEEE Trans. Instrum. Meas.*, vol. 70, pp. 1–13, 2021.
- [28] Y. Wang, Z. Shi, Y. Yu, S. Huang, and L. Chen, "Enabling angle-based positioning to 3GPP NR systems," in *Proc. 16th Workshop Positioning, Navigat. Commun. (WPNC)*, Oct. 2019, pp. 1–7.
- [29] D. He, X. Chen, L. Pei, F. Zhu, L. Jiang, and W. Yu, "Multi-BS spatial spectrum fusion for 2-D DOA estimation and localization using UCA in massive MIMO system," *IEEE Trans. Instrum. Meas.*, vol. 70, pp. 1–13, 2021.
- [30] Q. Liu, C. Gao, A. Xhafa, W. Gao, J. A. López-Salcedo, and G. Seco-Granados, "Performance analysis of GNSS + 5G hybrid positioning algorithms for smartphones in urban environments," *IEEE Trans. Instrum. Meas.*, vol. 73, pp. 1–9, 2024.
- [31] Q. Liu, C. Gao, R. Shang, W. Gao, J. A. López-Salcedo, and G. Seco-Granados, "Hybrid GNSS+ 5G position and rotation estimation algorithm based on TOA and unit vector of arrival in urban environment," *IEEE Trans. Instrum. Meas.*, vol. 73, 2024, Art. no. 9512908.
- [32] F. Ghaseminajm, M. Alsamdi, and S. S. Ikki, "Error bounds for localization in mmWave MIMO systems: Effects of hardware impairments considering perfect and imperfect clock synchronization," *IEEE Syst. J.*, vol. 16, no. 4, pp. 6350–6359, Dec. 2022.
- [33] O. Kolawole, A. Papazafiroopoulos, and T. Ratnarajah, "Impact of hardware impairments on mmWave mimo systems with hybrid precoding," in *Proc. IEEE WCNC*, Apr. 2018, pp. 1–6.
- [34] M. Henninger, S. Sengupta, S. Mandelli, and S. ten Brink, "Performance evaluation of array calibration for angle-of-arrival-based 5G positioning," in *Proc. WSA SCC 26th Int. ITG Workshop Smart Antennas 13th Conf. Syst., Commun., Coding*, Feb. 2023, pp. 1–6.
- [35] S. Monfared, T.-H. Nguyen, T. V. D. Vorst, P. D. Doncker, and F. Horlin, "Experimental demonstration of AoA estimation uncertainty for IoT sensor networks," in *Proc. IEEE 91st Veh. Technol. Conf. (VTC-Spring)*, May 2020, pp. 1–5.
- [36] H. Chen et al., "Modeling and analysis of OFDM-based 5G/6G localization under hardware impairments," *IEEE Trans. Wireless Commun.*, vol. 23, no. 7, pp. 7319–7333, Jul. 2024.
- [37] E. Y. Menta, N. Malm, R. Jäntti, K. Ruttik, M. Costa, and K. Leppänen, "On the performance of AoA-based localization in 5G ultra-dense networks," *IEEE Access*, vol. 7, pp. 33870–33880, 2019.
- [38] R. Pöhlmann, S. Zhang, E. Staudinger, S. Caizzone, A. Dammann, and P. A. Hoeher, "Bayesian in-situ calibration of multipoint antennas for DoA estimation: Theory and measurements," *IEEE Access*, vol. 10, pp. 37967–37983, 2022.
- [39] M. S. Bartlett, "Periodogram analysis and continuous spectra," *Biometrika*, vol. 37, nos. 1-2, pp. 1–16, Jun. 1950.
- [40] R. O. Schmidt, *A Signal Subspace Approach to Multiple Emitter Location Spectral Estimation*. Stanford, CA, USA: Stanford Univ., 1982.
- [41] R. Roy and T. Kailath, "Esprit-estimation of signal parameters via rotational invariance techniques," *IEEE Trans. Acoust., Speech, Signal Process.*, vol. 37, no. 7, pp. 984–995, Jul. 1989.
- [42] T. Yardibi, J. Li, P. Stoica, M. Xue, and A. B. Baggeroer, "Source localization and sensing: A nonparametric iterative adaptive approach based on weighted least squares," *IEEE Trans. Aerosp. Electron. Syst.*, vol. 46, no. 1, pp. 425–443, Jan. 2010.
- [43] W. Roberts, P. Stoica, J. Li, T. Yardibi, and F. A. Sadjadi, "Iterative adaptive approaches to MIMO radar imaging," *IEEE J. Sel. Topics Signal Process.*, vol. 4, no. 1, pp. 5–20, Feb. 2010.
- [44] J.-P. Delmas, "Asymptotically minimum variance second-order estimation for noncircular signals with application to DOA estimation," *IEEE Trans. Signal Process.*, vol. 52, no. 5, pp. 1235–1241, May 2004.
- [45] D. Malioutov, M. Cetin, and A. S. Willsky, "A sparse signal reconstruction perspective for source localization with sensor arrays," *IEEE Trans. Signal Process.*, vol. 53, no. 8, pp. 3010–3022, Aug. 2005.
- [46] H. Abeida, Q. Zhang, J. Li, and N. Merabtin, "Iterative sparse asymptotic minimum variance based approaches for array processing," *IEEE Trans. Signal Process.*, vol. 61, no. 4, pp. 933–944, 2012.
- [47] G. Yammine et al., "Experimental investigation of 5G positioning performance using a mmWave measurement setup," in *Proc. Int. Conf. Indoor Positioning Indoor Navigat. (IPIN)*, Nov. 2021, pp. 1–8.
- [48] 5G, *Study Channel Model for Frequencies From 0.5 to 100 GHz*, Standard ETSI TR138.901, V16.1.0, 3GPP, 2020.
- [49] E. Research. (2023). *Ettus Research Knowledge Base: USRP N300/N310*. Accessed: Jul. 19, 2023. [Online]. Available: <https://kb.ettus.com/N300/N310>
- [50] N. Instruments. (2023). *Product Documentation NI-2955*. Accessed: Jul. 19, 2023. [Online]. Available: <https://www.ni.com/docs/de-DE/bundle/usrp-2955-specs/page/specs.html>
- [51] A. Xhafa, F. Fabra, J. A. López-Salcedo, G. Seco-Granados, and I. Lapin, "Pathway to coherent phase acquisition in multi-channel USRP SDRs for direction of arrival estimation," in *Proc. 10th Int. Conf. Softw. Defined Syst. (SDS)*, Oct. 2023, pp. 1–8.
- [52] M. Viberg, M. Lanne, and A. Lundgren, "Calibration in array processing," in *Classical and Modern Direction-of-Arrival Estimation*. Amsterdam, The Netherlands: Elsevier, 2009, pp. 93–124.
- [53] A. B. Gershman, "Robust adaptive beamforming in sensor arrays," *Int. J. Electron. Commun.*, vol. 53, pp. 305–314, Mar. 1999.
- [54] S. M. Kay, *Fundamentals of Statistical Signal Processing: Estimation*. Upper Saddle River, NJ, USA: Prentice-Hall, 1993.
- [55] K. Shamaei and Z. M. Kassas, "A joint TOA and DOA acquisition and tracking approach for positioning with LTE signals," *IEEE Trans. Signal Process.*, vol. 69, pp. 2689–2705, 2021.
- [56] C. R. N. Athaudage and K. Sathananthan, "Cramer–Rao lower bound on frequency offset estimation error in OFDM systems with timing error feedback compensation," in *Proc. 5th Int. Conf. Inf. Commun. Signal Process.*, Dec. 2005, pp. 1231–1235.
- [57] S. L. Cardoso, A. da Costa, and A. dos Santos Gonçalves, "Analysis of absorption and reflection of electromagnetic waves on aluminum foil with cell phones," *ISCE: J. Innov. Stud. Character Edu.*, vol. 8, no. 1, pp. 26–34, 2024.
- [58] C. L. Dillard, "A study of rough surface scattering phenomena in the LMDS band (28 GHz)," Ph.D. dissertation, Fac. Virginia Polytech. Inst. State Univ., Blacksburg, VA, USA, 2003.
- [59] V. Pozzobon, W. Levasseur, K.-V. Do, B. Palpant, and P. Perré, "Household aluminum foil matte and bright side reflectivity measurements: Application to a photobioreactor light concentrator design," *Biotechnol. Rep.*, vol. 25, Mar. 2020, Art. no. e00399.
- [60] M. Sainz-Menchón, J. Gabirondo-López, I. González de Arrieta, T. Echàiz, and G. A. López, "Experimental and numerical study of the emissivity of rolled aluminum," *Infr. Phys. Technol.*, vol. 127, Dec. 2022, Art. no. 104380.



**Alda Xhafa** (Member, IEEE) received the B.Sc. degree in telecommunication engineering from the Polytechnic University of Tirana (UPT), Tirana, Albania, in 2015, and the M.Sc. degree in telecommunication engineering from the Universitat Politècnica de Catalunya (UPC), Barcelona, Spain, in 2017, and the Ph.D. degree in electrical engineering from the Universitat Autònoma de Barcelona (UAB), Barcelona, in 2024.

From March 2018 to September 2019, she was an Assistant Lecturer with the Department of Electronics and Telecommunications at the Faculty of Information Technology, UPT. During her Ph.D., she conducted a research stay at Airbus Defense and Space GmbH in Munich, where she worked on the generation and reception of 5G real signals for positioning, performing angular measurements using software-defined radio (SDR) equipment, and collecting and analyzing field measurements over commercial 5G networks. She has contributed to multiple research projects funded by the Spanish Agency of Research (AEI) and the European Space Agency (ESA). Her research interests include wireless communications, terrestrial, and nonterrestrial localization systems, and positioning with 5G/6G technologies.



**Fran Fabra** received the M.Sc. degree in telecommunication engineering and the master's degree in information and communication technologies from Universitat Politècnica de Catalunya (UPC), Barcelona, Spain, in 2007, and the Ph.D. degree from the Universitat Politècnica de Catalunya, Barcelona, in 2013.

He developed his Master's thesis on security in aeronautical mobile networks at TriaGnoSys GmbH, Munich, Germany. His Ph.D. dissertation was dedicated to the research of the GNSS-R concept toward remote sensing of the cryosphere. From December 2007 to December 2019, he was with the Earth Observation Research Group from the Institute of Space Sciences (ICE-CSIC/IEEC), Barcelona, Spain, working on applications of global navigation satellite systems for remote sensing of the Earth. Such experience ranged from the theoretical study of pioneering GNSS-R techniques to their experimental proof of concept and validation from real data analysis. He was also the main developer of the open-source wavy library for GNSS-R analysis and modeling. In November 2019, he joined as a Post-Doctoral Researcher with the Signal Processing for Communications and Navigation Group, Universitat Autònoma de Barcelona (UAB/IEEC), Spain, where he became an Associate Professor in May 2024. His current research interests lie in the field of statistical GNSS signal processing, LEO-PNT applications, SDR development, and antenna array analysis.



**Daniel Egea-Roca** (Member, IEEE) received the M.Sc. and Ph.D. degrees in electrical engineering from the Universitat Autònoma de Barcelona (UAB), Bellaterra, Barcelona, Spain, in 2012 and 2017, respectively.

During his Ph.D., he was involved in research projects funded by the European Commission (EC) and GSA, respectively. Furthermore, he did several visiting appointments, such as at Princeton University, Princeton, NJ, USA, hosted by Prof. H. Vincent Poor, and Hanyang University (South Korea) hosted by Prof. Sunwoo Kim. In 2017, he joined the Department of Telecommunications and Systems Engineering, UAB, as a Post-Doctoral Researcher. Since then, he has been involved in several research projects funded by the EC and European Space Agency (ESA). Since 2023, he has been with the Institute of Space Studies of Catalonia (IEEC). He authored around 20 publications and received three best paper/presentation awards. His research interests include the area of signal processing and its application in threat detection and integrity techniques for GNSS receivers. In the last years, he has been involved in the research of GNSS signal design and LEO-PNT.



**José A. López-Salcedo** (Senior Member, IEEE) received the M.Sc. and Ph.D. degrees in telecommunication engineering from the Universitat Politècnica de Catalunya, Barcelona, Spain, in 2001 and 2007, respectively.

Since 2006, he has been with the Universitat Autònoma de Barcelona, Barcelona, where he is currently a Professor, and served as the Coordinator of the Telecommunications Engineering degree, from 2011 to 2019. He is also with the Institute of Spatial Studies of Catalonia (IEEC) and Co-Founder of the start-up company Loctio. He has held several visiting appointments at the University of Illinois Urbana-Champaign, the University of California at Irvine, Irvine, CA, USA, and the European Commission Joint Research Center. He has been the principal investigator of more than 25 research projects, most of them funded by the European Space Agency (ESA) on topics dealing with signal processing for GNSS receivers. His research interests lie in the field of signal processing for communications and navigation, with emphasis on the convergence between GNSS, 5G/6G, and LEO satellites for Positioning, Navigation, and Timing (PNT).

Dr. López-Salcedo serves as Secretary and Treasurer of the Spanish Chapter of the IEEE Aerospace and Electronic Systems Society (AESS), member of the Editorial Committee of the Korean Institute of Positioning, Navigation and Timing (IPNT) and member of the IEEE Signal Processing Society Sensor Array and Multichannel Technical Committee (SAM TC).



**Gonzalo Seco-Granados** (Fellow, IEEE) received the Ph.D. degree in telecommunications engineering from the Universitat Politècnica de Catalunya, Barcelona, Spain, in 2000, and the M.B.A. degree from the IESE Business School, Barcelona, in 2002.

From 2002 to 2005, he was a Member of the European Space Agency, where he was involved in the design of the Galileo system. He is currently a Professor with the Department of Telecommunication, Universitat Autònoma de Barcelona, Barcelona, where he served as Coordinator of the Telecommunications Engineering degree, from 2007 to 2010, and as the Vice Dean of the Engineering School, from 2011 to 2019. In 2015, 2019, and 2022, he was a Fulbright Visiting Scholar at the University of California, Irvine, CA, USA. He is also with the Institute of Spatial Studies of Catalonia (IEEC) and an ICREA Academia fellow. He is the Co-Founder of Loctio, a start-up providing low-energy GNSS positioning solutions for IoT. He has more than 370 publications in his research areas and holds five related patents. His research interests include GNSS, and beyond 5G integrated communications, localization, and sensing.

Dr. Seco-Granados serves as a member of the IEEE Signal Processing Society Sensor Array and Multichannel Technical Committee (SAM TC), and of the EURASIP Signal Processing for Multisensor Systems Technical Committee, since 2018 and 2022, respectively. Since 2019, he has been President of the Spanish Chapter of the IEEE Aerospace and Electronic Systems Society. He received the 2021 IEEE Signal Processing Society's Best Paper Award.